

RESEARCH ARTICLE

10.1002/2016WR019222

Key Points:

- Nonlinear interface conditions in the quasilinear formulation are solved for inhomogeneities in the vadose zone
- Patterns in pressure head distribution and pathline geometry are analyzed across variations in recharge rate
- A shift in recharge rate becomes evident by changes in pressure around finer grained inhomogeneities well above groundwater

Correspondence to:

D. R. Steward,
steward@ksu.edu

Citation:

Steward, D. R. (2016), Analysis of vadose zone inhomogeneity toward distinguishing recharge rates: Solving the nonlinear interface problem with Newton method, *Water Resour. Res.*, 52, 8756–8774, doi:10.1002/2016WR019222.

Received 17 MAY 2016

Accepted 20 OCT 2016

Accepted article online 1 NOV 2016

Published online 18 NOV 2016

Analysis of vadose zone inhomogeneity toward distinguishing recharge rates: Solving the nonlinear interface problem with Newton method

David R. Steward¹

¹Department of Civil Engineering, Kansas State University, Manhattan, Kansas, USA

Abstract Recharge from surface to groundwater is an important component of the hydrological cycle, yet its rate is difficult to quantify. Percolation through two-dimensional circular inhomogeneities in the vadose zone is studied where one soil type is embedded within a uniform background, and nonlinear interface conditions in the quasilinear formulation are solved using Newton’s method with the Analytic Element Method. This numerical laboratory identifies detectable variations in pathline and pressure head distributions that manifest due to a shift in recharge rate through in a heterogeneous media. Pathlines either diverge about or converge through coarser and finer grained materials with inverse patterns forming across lower and upper elevations; however, pathline geometry is not significantly altered by recharge. Analysis of pressure head in lower regions near groundwater identifies a new phenomenon: its distribution is not significantly impacted by an inhomogeneity soil type, nor by its placement nor by recharge rate. Another revelation is that pressure head for coarser grained inhomogeneities in upper regions is completely controlled by geometry and conductivity contrasts; a shift in recharge generates a difference Δp that becomes an additive constant with the same value throughout this region. In contrast, shifts in recharge for finer grained inhomogeneities reveal patterns with abrupt variations across their interfaces. Consequently, measurements aimed at detecting shifts in recharge in a heterogeneous vadose zone by deciphering the corresponding patterns of change in pressure head should focus on finer grained inclusions well above a groundwater table.

1. Introduction

Recharge is that portion of precipitation that percolates downward in the vadose zone, past the root zone, and becomes the infiltrated source of groundwater. Recharge provides a hydrologic link between surficial and groundwater processes [Steward et al., 2011] and its rate is clearly important; e.g., recharge focused through streambeds of ephemeral rivers provide a potential avenue to refill depleting aquifers [Ahring and Steward, 2012]. And yet quantification of recharge rates is difficult. This study examines recharge through a heterogeneous vadose zone toward identifying the types of measurements that are capable of detecting changes in the rate of recharge.

Water moves more readily through moist soils than through dry soils. This property is captured by expressing the hydraulic conductivity $K(p)$ as a function of the pressure head p , from the Bernoulli [1738] equation:

$$h = p + z, \quad p = \frac{P}{\rho g} \tag{1}$$

where h is vadose zone head, the z -coordinate axis is directed upward against gravity, and the soil water pressure P decreases as a soil dries. While many functional forms exist, it is convenient to use the Gardner [1958] equation:

$$K(p) = K_s e^{ap} \tag{2}$$

where a is the sorptive number, and the hydraulic conductivity takes on its saturated value K_s when the vadose zone reaches the limit of full saturation ($p = 0$). This equation has been widely adopted, and the representative soil properties in Table 1 were aggregated as ensemble averages for each soil type from the specified references.

Table 1. Representative Soil Properties^a for Hydraulic Conductivity in the Gardner Equation, (2)

Soil Type	Saturated Conductivity K_s (m/d)	Sorptive Number a (1/m)
Silt	0.02	2
Fine sand	1	5
Coarse sand	35	25

^aAdapted from Bresler [1978, Table 1], Rockhold et al. [1997, Table 1], Khaleel and Relyea [2001, Table 3], Varado et al. [2006, Table 1], and Zhu and Warrick [2012, Table 1].

A quasilinear approach using the Gardner equation was pioneered by Philip [1968] to study recharge around objects in the vadose zone. The exclusion problem of seepage near a cavity has been formulated for a circular cylinder [Philip et al., 1989a], a sphere [Knight et al., 1989], a parabola or paraboloid [Philip et al., 1989b], and an ellipse [Kuhlman and Warrick, 2008]. The Analytic Element Method, which is used later, was developed by Strack [1989, 2003] for groundwater flow and provides nearly exact solutions to saturated inhomogeneities filled

with a different type of soil than the background. The first application of the AEM to the unsaturated vadose zone was performed by Warrick and Knight [2002, 2004] to study an inhomogeneity of circular or spherical geometry. These developments require all soil types to have the same sorptive number due to the existence of a nonlinear condition, (24), that becomes linear when a is uniform.

Such existing quasilinear solutions are shown in Figure 1 for two-dimensional recharge seeping through silt or coarse sand embedded within a background of fine sand, with the properties of Table 1 except all soils use the sorptive number for fine sand in $K(p)$, (2). The illustrated lines of constant pressure head and the pathlines follow those in Warrick and Knight [2002, Figures 3 and 4]. All existing solutions, such as these and those in the references, place the inhomogeneity into a background of uniform pressure head associated with constant downward seepage a long distance from the object [Philip, 1990, equation 1.3] (e.g., the pressure head $p_0 = -1.64$ m, (16), for fine sand in Figure 1).

This study analyzes patterns in the geometry of pathlines and preferential flow paths, and the distribution of pressure head in the vadose zone that exist as recharge seeps through representative soils. The goal is to identify those patterns that manifest change across a shift in recharge and provide indicators capable of quantifying its rate. Important, unresolved questions exist in vadose zone seepage. How does the sorptive number for typical soils impact recharge through inhomogeneities? How does the vertical placement of an inhomogeneity in the vadose zone impact its solution? And, what detectable changes in pressure head and pathlines distributions might be expected to manifest across variation in recharge rates for heterogeneous soils in the vadose zone? These questions are resolved in this study using Newton's method to obtain nonlinear solutions in the vadose zone with the Analytic Element Method, which is presented next.

2. Methods

Formulation of the problem for two-dimensional flow in a vertical plane and methods to solve the nonlinear interface problem follow, with implementation details deferred to Appendix A. Use of the quasilinear

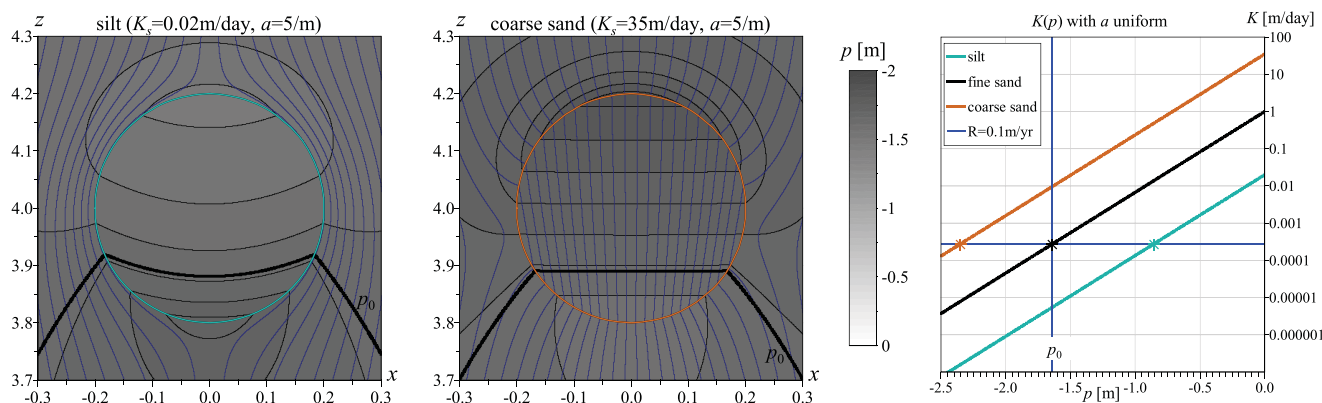


Figure 1. Circular inhomogeneity of silt or coarse sand embedded in fine sand, with a sorptive number uniform across all porous media following Warrick and Knight [2002]. Dark blue lines are streamlines, and black lines are isobars with contour interval of pressure head $\Delta p = 0.05$ m. The thicker dark line at $p = p_0$ corresponding to the fine sand's gravity drainage where conductivity K equals recharge rate R .

formulation in the Analytic Element Method follow *Warrick and Knight* [2002, 2004] for variable saturated conductivity, and the linearization methods used by *Bakker and Nieber* [2004a, 2004b] for variable sorptive number are extended to the nonlinear Newton method. Readers interested in proceeding directly to results and discussion are directed to section 3.

2.1. The Quasilinear Formulation

Vadose zone processes are studied within a quasilinear formulation, and the significant developments are briefly summarized next. Flow is governed by two conditions: (1) the *Darcy* [1856] law, which relates specific discharge to head, (1):

$$q_x = -K(p) \frac{\partial p}{\partial x}, \quad q_z = -K(p) \frac{\partial p}{\partial z} - K(p) \tag{3}$$

and (2) conservation of mass, which is $\frac{\partial q_x}{\partial x} + \frac{\partial q_z}{\partial z} = 0$ for steady flow in a vertical plane. Together, these give the *Richards* [1931] equation

$$\frac{\partial}{\partial x} \left[K(p) \frac{\partial p}{\partial x} \right] + \frac{\partial}{\partial z} \left[K(p) \frac{\partial p}{\partial z} \right] = - \frac{\partial K(p)}{\partial z} \tag{4}$$

The *Kirchhoff* [1894] transformation facilitates organization of these partial derivatives in terms of a matrix flux potential, *F*:

$$F = \int_{-\infty}^p K(\bar{p}) d\bar{p} \quad \rightarrow \quad \begin{cases} \frac{\partial F}{\partial x} = K \frac{\partial p}{\partial x} \\ \frac{\partial F}{\partial z} = K \frac{\partial p}{\partial z} \end{cases} \tag{5}$$

to give

$$\frac{\partial^2 F}{\partial x^2} + \frac{\partial^2 F}{\partial z^2} = - \frac{\partial K(p)}{\partial z} \tag{6}$$

The right-hand side of this equation is rearranged

$$\frac{\partial K}{\partial z} = \frac{dK}{dp} \frac{\partial p}{\partial z} = \frac{dK}{dp} \frac{1}{K} \frac{\partial F}{\partial z} = a \frac{\partial F}{\partial z} \tag{7}$$

using the *z* derivative in (5) with the Gardner equation (2). Together, the last two equations give the quasilinear equation

$$\frac{\partial^2 F}{\partial x^2} + \frac{\partial^2 F}{\partial z^2} = -a \frac{\partial F}{\partial z} \tag{8}$$

which has been broadly adopted for vadose zone studies [*Pullan, 1990*]. A change of variables transformation [*Wooding, 1968*]

$$F = \Phi e^{-kz}, \quad \Phi = F e^{kz}, \quad k = \frac{a}{2} \tag{9}$$

rearranges the quasilinear equation to give the modified Helmholtz equation:

$$\frac{\partial^2 \Phi}{\partial x^2} + \frac{\partial^2 \Phi}{\partial z^2} = k^2 \Phi \tag{10}$$

Solutions are obtained using functions Φ that satisfy this equation. Boundary conditions for pressure head may be expressed in terms of Φ using the transformation

$$\Phi = F_s e^{k(z+2p)} \quad \leftrightarrow \quad p = \frac{1}{2k} \ln \frac{\Phi e^{-kz}}{F_s} \tag{11}$$

where F_s is the matrix flux potential at $p = 0$. This expression arises from the change of variables (9) together with the Kirchhoff transformation (5) integrated with the Gardner equation (2):

$$F = F_s e^{2kp}, \quad F_s = \frac{K_s}{a} \tag{12}$$

Similarly, boundary conditions for specific discharge are related to Φ using

$$q_x = -e^{-kz} \frac{\partial \Phi}{\partial x}, \quad q_z = -e^{-kz} \left(\frac{\partial \Phi}{\partial z} + k\Phi \right) \tag{13}$$

This expression follows from Darcy's law (3) using the derivatives of the Kirchhoff transformation in (5) with the change of variables (9) along with $F = K/a$ from (12) and (2).

Use of the quasilinear formulation to solve vadose zone problems is illustrated for the uniform recharge occurring as a background flow into which inhomogeneities are located. A general solution to (10) for one-dimensional seepage and its specific discharge (13) are

$$\Phi = c_1 e^{-kz} + c_2 e^{kz}, \quad q_z = -c_2 2k \tag{14}$$

The coefficients c_1 and c_2 are found by setting pressure head to $p = 0$ at the elevation $z = 0$ of the groundwater table in (11) and setting the specific discharge equal to minus the recharge rate R , similar to *Rockhold et al.* [1997], to give

$$\Phi(z=0) = F_s, \quad q_z = -R \rightarrow \begin{cases} c_1 = F_s - \frac{R}{2k} \\ c_2 = \frac{R}{2k} \end{cases} \tag{15}$$

An asymptotic limit exists above the groundwater table [*Raats and Gardner*, 1974] where $\Phi \rightarrow \frac{R}{2k} e^{kz}$ and pressure head (11) approaches

$$p_0 = \lim_{z \gg 0} p = \frac{1}{2k} \ln \frac{R}{2kF_s} = \frac{1}{a} \ln \frac{R}{K_s} \tag{16}$$

This gives the background suction pressure head for fine sand of $p_0 = -1.64$ m in Figure 1 into which the inhomogeneity is placed, a value consistent with *Rucker et al.* [2005].

Solutions to the modified Helmholtz equation, (10), for a circular inhomogeneity are given by separation of variables in circular coordinates, $\Phi(r, \theta)$ in terms of the modified Bessel functions I_n and K_n [*Moon and Spencer*, 1961]. These functions are evaluated in the domains outside or inside the element of radius r_0 where they remain finite, and the separated solutions provides influence functions that are linearly combined:

$$\Phi = \begin{cases} \sum_{n=0}^N c_n^{K \cos} K_n(kr) \cos n\theta + \sum_{n=1}^N c_n^{K \sin} K_n(kr) \sin n\theta & (r \geq r_0) \\ \sum_{n=0}^N c_n^{I \cos} I_n(kr) \cos n\theta + \sum_{n=1}^N c_n^{I \sin} I_n(kr) \sin n\theta & (r < r_0) \end{cases} \tag{17}$$

where the coefficients $c_n^{K \cos}$, $c_n^{K \sin}$, $c_n^{I \cos}$, and $c_n^{I \sin}$ must be adjusted to provide a solution. Linear superposition of these influence functions is illustrated in Figure 2, where the vectors are directed toward decreasing Φ . This gradient of these functions is needed to evaluate the specific discharge, and presented later in (A6). Extension to the study of three-dimensional elements requires separable solutions for spherical coordinates, such as presented in *Warrick and Knight* [2004].

2.2. Formulating a Solution to the Nonlinear Interface Condition

The heterogeneity of soils is modeled using a conceptualization of porous media consistent with the embedded matrix of *Dagan* [1979], where elements composed of one soil type with specific properties are placed within a uniform background with a different set of soil properties. This is illustrated in Figure 2 where an inhomogeneity with saturated conductivity K_s^- and sorptive number a^- is placed within a background with K_s^+ and a^+ . This circular element i is centered at (x_c, z_c) with radius r_0 . While one element is shown in Figure 1, heterogeneity composed of the superposition of $i = 1$ to l elements is studied later for

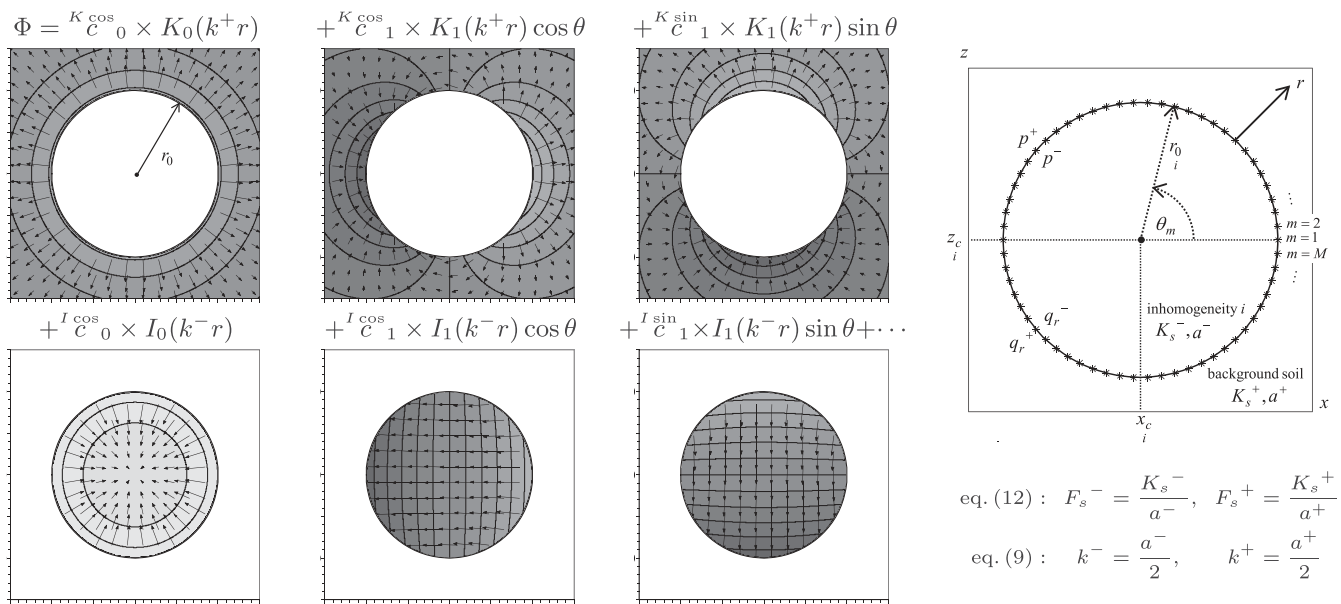


Figure 2. The inhomogeneity's linear superposition of influence functions, (17), and element geometry used in the Analytic Element Method to solve the nonlinear interface condition.

an ensemble of inclusions using superposition of the individual inhomogeneities. The developments necessary to solve this problem follow with details for implementing the solution deferred to Appendix A.

A comprehensive solution for a collection of inhomogeneities is obtained by combining the contributions from all elements. At point (x, z) outside all inhomogeneities, the Helmholtz solution (17) is summed across the I elements with background uniform seepage (14) to give

$$\Phi = \sum_{i=1}^I \sum_{n=0}^N {}^K \mathcal{C}_i^{\cos} n K_n(k^+ r_i) \cos n \theta_i + \sum_{n=1}^N {}^K \mathcal{C}_i^{\sin} n K_n(k^+ r_i) \sin n \theta_i + c_1 e^{-k^+ z} + c_2 e^{k^+ z} \quad (18)$$

where the distance to the center of the i th element is

$$r_i = \sqrt{(x - x_c)^2 + (z - z_c)^2} \quad (19)$$

and θ_i is the angle measured about its center. It is convenient when obtaining the solution for element i to separate its coefficients from those for other elements

$$\Phi = \sum_{n=0}^N {}^K \mathcal{C}_i^{\cos} n K_n(k^+ r_i) \cos n \theta_i + \sum_{n=1}^N {}^K \mathcal{C}_i^{\sin} n K_n(k^+ r_i) \sin n \theta_i + \Phi_i^{\text{add}} \quad (20a)$$

using the additional function [Steward, 2015]:

$$\Phi_i^{\text{add}} = \sum_{j \neq i}^I \sum_{n=0}^N {}^K \mathcal{C}_j^{\cos} n K_n(k^+ r_j) \cos n \theta_j + \sum_{n=1}^N {}^K \mathcal{C}_j^{\sin} n K_n(k^+ r_j) \sin n \theta_j + c_1 e^{-k^+ z} + c_2 e^{k^+ z} \quad (20b)$$

The solution at a location inside element i is given by

$$\Phi = \sum_{n=0}^N \zeta_i^{\cos} n l_n \left(k^- r_i \right) \cos n \theta + \sum_{n=1}^N \zeta_i^{\sin} n l_n \left(k^- r_i \right) \sin n \theta + \zeta_i^D 1 e^{-k^- z} + \zeta_i^D 2 e^{k^- z} \tag{21}$$

This contains the separated solution (17) with (14) since this one-dimensional variation predominates some problems, such as when the same soil properties are specified inside and outside an inhomogeneity (used later in Figures 4–6). Note that each solution satisfies the modified Helmholtz equation, (10), with the term k^+ or k^- in the domain in which it is evaluated. A short-hand notation is adopted when formulating a solution for element i , where the underscript i is implied but not specified in the following equations.

The conditions that must be satisfied across the interface of an inhomogeneity are specified at control point m located at angle

$$\theta_m = 2\pi \frac{m-1}{M} \quad (m=1, 2, \dots, M) \tag{22}$$

in Figure 2, where M is the number of evenly spaced control points. A nonlinear condition exists across this interface from continuity of pressure head

$$p^+ = p^-, \quad \begin{aligned} p^+ &= \frac{1}{2k^+} \ln \frac{e^{-k^+ z} \Phi^+}{F_s^+} \\ p^- &= \frac{1}{2k^-} \ln \frac{e^{-k^- z} \Phi^-}{F_s^-} \end{aligned} \tag{23}$$

using (11). This gives the first interface condition:

$$f_m^{(1)} = \left(\frac{e^{-k^+ z_m} \Phi_m^+}{F_s^+} \right)^{\gamma^+} - \left(\frac{e^{-k^- z_m} \Phi_m^-}{F_s^-} \right)^{\gamma^-} \tag{24}$$

where γ^+ and γ^- are chosen to be less than or equal to one:

$$\begin{aligned} \gamma^+ &= \frac{k^-}{k^+}, \gamma^- = 1 & (k^- \leq k^+) \\ \gamma^+ &= 1, \gamma^- = \frac{k^+}{k^-} & (k^- > k^+) \end{aligned} \tag{25}$$

A Robin condition also exists from the normal component of the specific discharge vector outside and inside the element:

$$q_r^+ = q_r^-, \quad \begin{aligned} q_r^+ &= -e^{-k^+ z} \left[(k^+ \sin \theta) \Phi^+ + \frac{\partial \Phi^+}{\partial r} \right] \\ q_r^- &= -e^{-k^- z} \left[(k^- \sin \theta) \Phi^- + \frac{\partial \Phi^-}{\partial r} \right] \end{aligned} \tag{26}$$

using (13). This gives the second interface condition:

$$\begin{aligned} f_m^{(2)} &= -e^{-k^+ z_m} \left[(k^+ \sin \theta_m) \Phi_m^+ + \frac{\partial \Phi_m^+}{\partial r} \right] \\ &+ e^{-k^- z_m} \left[(k^- \sin \theta_m) \Phi_m^- + \frac{\partial \Phi_m^-}{\partial r} \right] \end{aligned} \tag{27}$$

The sewing theorem [Courant, 1950, Theorem 2.5] is adapted to this problem to stitch together the function Φ and its derivatives outside and inside an inhomogeneity. This stitching at the control points seeks a solution for $f_m^{(1)}$, (24), and $f_m^{(2)}$, (27), that approaches a minimum across all M control points. Due to the nonlinear interface condition, a nonlinear solver is applied using the iterative Newton's method. This is accomplished for element i by fixing the coefficients for all other elements in the additional function (20b), and organizing the coefficient vector and known vector in

$$\mathbf{c} = \begin{bmatrix} K \cos \\ C_n \\ K \sin \\ C_n \\ i \cos \\ C_n \\ i \sin \\ C_n \\ 1, D \\ C_1 \\ 1, D \\ C_2 \end{bmatrix}, \quad \mathbf{f} = \begin{bmatrix} f_m^{(1)} \\ f_m^{(2)} \end{bmatrix} \quad (28a)$$

where initial coefficient values are set using (A9). Newton’s method provides an iterative method to compute changes in the coefficients \mathbf{c} from the value of the functions \mathbf{f} at iterate l :

$$\mathbf{J}_{l,j}(\Delta \mathbf{c})_l = -\mathbf{f}_l \quad (28b)$$

where the derivatives are specified by the Jacobian matrix:

$$\mathbf{J} = \begin{bmatrix} \frac{\partial f_m^{(1)}}{\partial C_n} & \frac{\partial f_m^{(1)}}{\partial C_n} & \frac{\partial f_m^{(1)}}{\partial C_n} & \frac{\partial f_m^{(1)}}{\partial C_n} & \frac{\partial f_m^{(1)}}{\partial C_1} & \frac{\partial f_m^{(1)}}{\partial C_2} \\ \frac{\partial f_m^{(2)}}{\partial C_n} & \frac{\partial f_m^{(2)}}{\partial C_n} & \frac{\partial f_m^{(2)}}{\partial C_n} & \frac{\partial f_m^{(2)}}{\partial C_n} & \frac{\partial f_m^{(2)}}{\partial C_1} & \frac{\partial f_m^{(2)}}{\partial C_2} \end{bmatrix} \quad (28c)$$

and the expressions necessary to evaluate these derivatives are found in (A11). This system of $2M$ equations with $4(N + 1)$ coefficients is solved using least squares following the overspecification principle of *Janković and Barnes* [1999] with more conditions than unknowns. The nonlinear condition $f_m^{(1)}$, (24), may alternately be solved by linearization [*Bakker and Nieber*, 2004a, 2004b].

Iteration for element i continues by updating \mathbf{J} and \mathbf{f} using the next estimate for coefficients until only small changes occur between successive iterates. This is repeated for all l elements using Gauss-Seidel with details presented in Appendix A. The solution was implemented in Scilab 5.4.0 on Beocat, a grid computing cluster at Kansas State University, and the numerical accuracy is reported in Table 2, which demonstrates that nearly exact solutions are achieved. In particular, the root-mean-square error of pressure head in $f_m^{(1)}$ across all control points for all inhomogeneities is less than $\Delta p/4500$, a small fraction of the contour interval 0.05 m used to visual isobars in Figures 1–5, and the rmse of the normal component of specific discharge in $f_m^{(2)}$ is less than $R/30,000$, a small fraction of the recharge rate.

3. Results and Discussion

3.1. An Inhomogeneity With Representative Soil Properties in a Background of Uniform Pressure Head

The new nonlinear solution methods facilitate study of seepage around and through inhomogeneities as illustrated in Figure 3 for silt and coarse sand embedded within a background of fine sand. This example utilizes the same soil types and settings as Figure 1, however, the representative soil properties in Table 1 are now applied with sorptive number varying by soil type. Both figures use elements of radius $r_0 = 0.2$ m centered at $z_c = 4$ m above a groundwater table where a uniform background pressure p_0 exists. Pathlines track particles beginning at evenly spaced locations along the top of each figure with step sizes $1/10,000$ the size

Table 2. Nearly Exact Solutions for $f_m^{(1)}$, (24), and $f_m^{(2)}$, (27), Reported as the Root-Mean-Square Error of the Differences in Pressure Head and Normal Component of the Specific Discharge Across the Interface of Inhomogeneities, Summed for All Control Points of All Inhomogeneities

Figures (Recharge Rate)	Soil Type	N	M	$p^+ - p^-$ (m)			$q_r^+ - q_r^-$ (m/d)		
				Silt	Fine Sand	Coarse Sand	Silt	Fine Sand	Coarse Sand
1 ($R = 0.1$ m/yr)		8	51	4.53×10^{-13}		7.27×10^{-11}	7.66×10^{-14}		8.94×10^{-14}
3 ($R = 0.1$ m/yr)		8	51	3.01×10^{-13}		1.11×10^{-5}	8.77×10^{-15}		2.00×10^{-9}
4 ($R = 0.1$ m/yr)		8	51	5.98×10^{-13}	4.69×10^{-18}	5.14×10^{-9}	6.41×10^{-13}	1.60×10^{-18}	8.96×10^{-9}
5,6 ($R = 0.05$ m/yr)		16	99	4.78×10^{-7}	4.17×10^{-19}	1.49×10^{-6}	2.97×10^{-9}	4.92×10^{-20}	3.84×10^{-9}
5,6 ($R = 0.1$ m/yr)		16	99	2.46×10^{-7}	4.12×10^{-19}	1.52×10^{-6}	2.47×10^{-9}	5.08×10^{-20}	7.69×10^{-9}
5,6 ($R = 0.2$ m/yr)		16	99	9.92×10^{-8}	3.16×10^{-19}	1.56×10^{-6}	2.89×10^{-9}	4.85×10^{-20}	1.54×10^{-8}

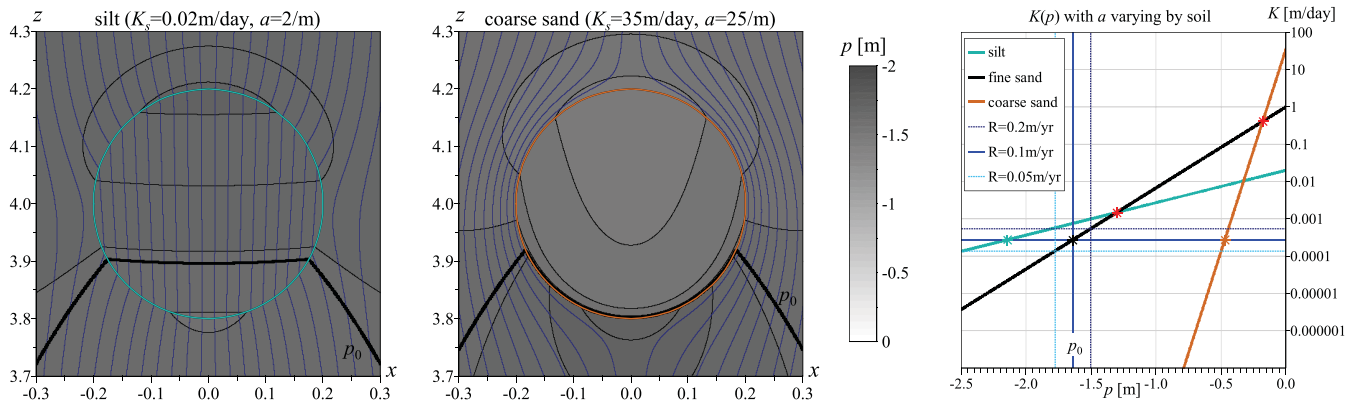


Figure 3. Inhomogeneity with a sorptive number varying by soil following Table 1, shown for recharge $R = 0.1$ m/yr.

of the figure. Isobars at $\Delta p = 0.05$ m were contoured from a 400×400 grid where Φ , (18) or (21), was computed at each grid point and then converted to p , (11). Clearly, differences are observed in both the pressure head and pathline distributions as the sorptive number changes.

The graph of hydraulic conductivity $K(p)$ in Figure 3 illustrates the constitutive soil properties. In the limiting case a large distance above the groundwater table, pressure head becomes $p_0 = \frac{1}{a} \ln \frac{R}{K_s}$, (16), as $K = R = 0.1$ m/yr and the isobars with this $p_0 = -1.64$ m for fine sand are shown for each inhomogeneity. Likewise, if the entire domain was filled with silt this equation would give a gravity drainage pressure head of -2.14 m, and -0.47 m for coarse sand using the soil properties in Table 1. (These gravity drainage values are indicated with markers on the $K(p)$ curves in Figure 3.) Within inhomogeneities, pressure head decreases for silt and increases for coarse sand as it transitions toward their gravity drainage values with increasing elevation. Yet it is observed that along the boundaries of each inhomogeneity either the top is higher than the p_0 of background fine sand and the bottom is lower, or vice versa (for both Figures 1 and 3). And so the background provides control over the range across which pressure head may fluctuate within a finer or coarser grained material embedded in the background soil.

These variations in pressure head distribution influence pathlines as seepage moves downward through and around an inhomogeneity. The $K(p)$ curve for silt in Figure 3 intersects the line of pressure head p_0 at a larger value of $K > R$ than that of fine sand. Thus, seepage moves more readily within the silt and the pathlines converge through this object. For the coarse sand, its $K(p)$ curve intersects p_0 at a very small value for K below the displayed values, and the object becomes nearly impermeable with pathlines diverging as seepage is transported around it. Thus, the variations in $K(p)$ of a finer grained soil may draw water toward and through it, while a coarser grained soil may repel water for an inhomogeneity located in a region of gravity drainage. The question addressed next is, what happens when an object is placed near a groundwater table where this background uniform pressure does not exist?

3.2. The Preponderant Progression of Pressure Head Toward Gravity Drainage Above a Groundwater Table, With Inverse Patterns of Diverging and Converging Pathlines

The impact of the vertical placement of an inhomogeneity is examined next by moving it to be in close proximity to the groundwater table, which is located at $z = 0$. The objects in Figure 4 share the geometry of those in Figure 3 with radius $r_0 = 0.2$ m, however, they are centered at elevation $z_c = 0.3$ m. The soil properties from Table 1 are also used with the same seepage rate R as previous examples. Note that the summation of the background flow plus the inhomogeneity, (20), matches the bottom boundary condition of atmospheric pressure head $p = 0$ very well. (This pressure head at $z = 0$ is within $\pm 2 \times 10^{-5}$ m, a very small fraction $\Delta p/2500$ of the contour interval).

This figure identifies an intriguing phenomenon: the pressure head near a groundwater table decreases in the upward direction toward its gravity drainage p_0 value; with a one-dimensional variation that is not influenced by the presence or absence of an inhomogeneity. Figure 4, middle shows the one-dimensional pressure head distribution occurring when the entire domain is filled with fine sand. This figure clearly illustrates that the same distribution in pressure head occurs regardless of the inclusion's soil type. Note

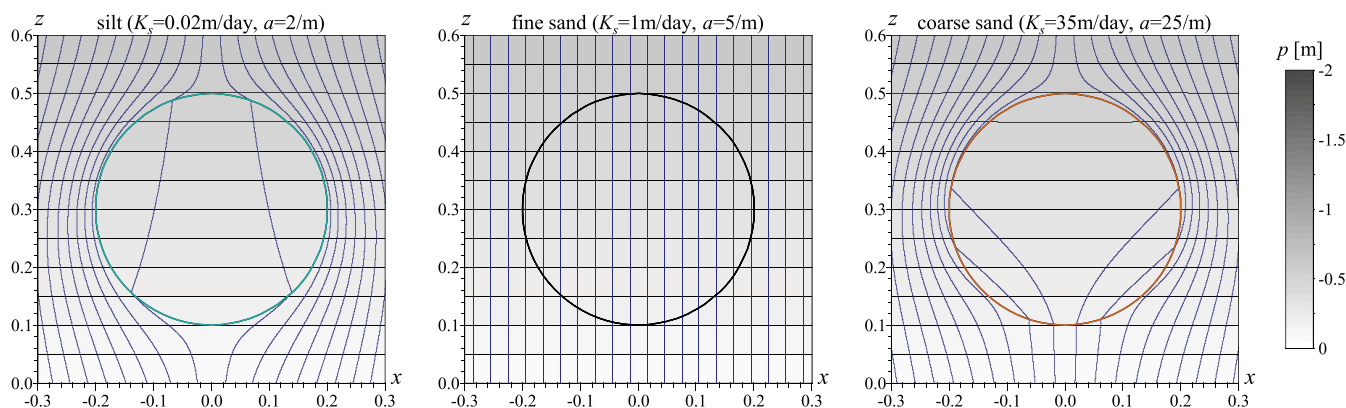


Figure 4. Inhomogeneity placed close to the groundwater table (where $p = 0$ at $z = 0$), shown for recharge $R = 0.1$ m/yr.

that sewing together the interior (21) and exterior (20) solutions across the interface enables a nearly exact solution for continuity of both pressure and the normal component of flow, as shown in Table 2.

The pathlines are influenced by the increasing hydraulic conductivity occurring with increasing pressure head as particles progress toward the groundwater table (along the top $p \approx -0.6$ m to 0 at the bottom). And these influences manifest themselves differently through the $K(p)$ distributions for each soil type. Clearly, pathlines form straight vertical lines when the domain is filled entirely with fine sand. Within the range of pressure head in the displayed region, the conductivity of silt is less than that of fine sand (shown in the graph of Figure 3). Thus, seepage occurs less readily in the silt and pathlines diverge around the object, and the transverse spreading increasing as particles travel downward toward the groundwater table. For coarse sand, its conductivity is less than fine sand until the two $K(p)$ curves meet at $p = -0.18$ m (shown by a red marker in Figure 3) and then its conductivity becomes higher than the background. This is observed in diverging pathlines around the top of the coarse sand and converging pathlines within its lower portion.

In summary, an inhomogeneity placed near a groundwater table may produce no discernible evidence of itself within the distribution of pressure head, yet it may significantly alter pathlines and the trajectories of water particles. And, the divergence or convergence of pathlines through and around an inhomogeneity form inverse patterns as an object in the region of uniform background pressure in Figure 3 is placed close to a groundwater table in Figure 4.

3.3. Pressure Head and Pathlines in a Heterogeneous Vadose Zone

The distributions of pressure head and pathlines have been clearly shown to be influenced by an inhomogeneity's soil properties, and also by its vertical placement. The next questions addressed are: how do these patterns manifest in a heterogeneous porous media? And, how do they change across shifts in recharge rates? A numerical laboratory is developed to study heterogeneity, which places the individual objects in Figures 3 and 4 in close proximity to other inhomogeneities. The simulated media in Figure 5 contains $I = 150$ elements in two zones of width 5 m and between elevations 0.05–2 m and 3–5 m. Their radii vary within $r_0 \in [0.05–0.5]$ m and they are randomly located to avoid intersections with a minimum spacing of 0.05 m between objects. This particular realization illustrates the impact of heterogeneity near a groundwater table and within a region of uniform background pressure, and serves as an example for future studies of other randomly generated configurations.

A domain filled entirely with the background fine sand is illustrated in the middle cutout sections shown between $x = -0.5$ to 0.5 m. Its pressure head varies as the one-dimensional field, (14), from $p = 0$ toward p_0 with increasing elevation; and provide the background into which the individual elements were inserted in Figures 3 and 4. Results are shown for three different recharge rates: the middle corresponds to $R = 0.1$ m/yr of the previous figures, and recharge is decreased and increased by a factor of 2 in the top and bottom figures. The gravity drainage pressure p_0 where $K = R$, (16), varies with shifts in recharge, as illustrated in the graph of Figure 3. And pathlines remain vertical lines for this uniform soil.

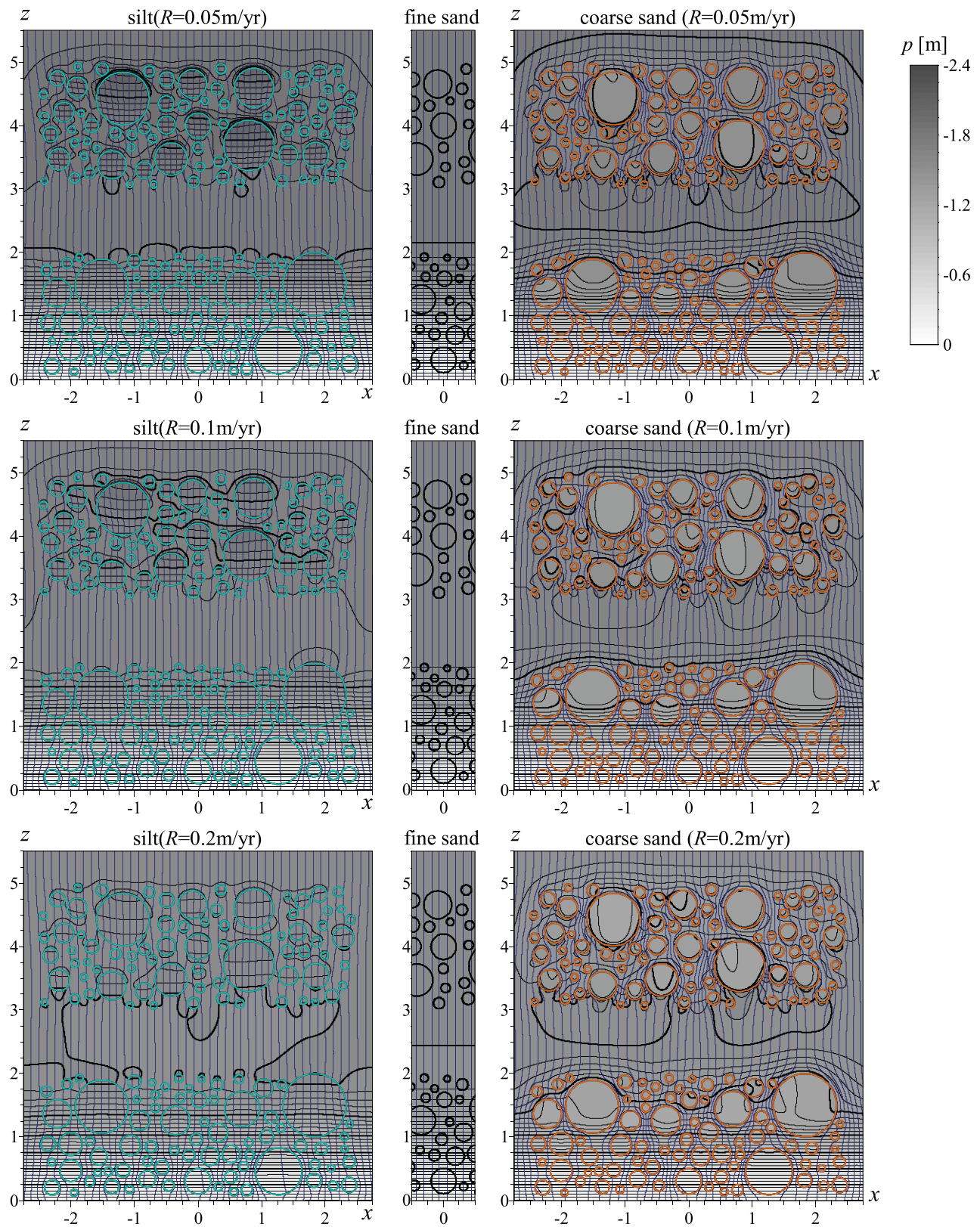


Figure 5. Inhomogeneities located within two different zones in fine sand, shown for different recharge rates. Contour intervals for pressure head are 0.05 m with thicker lines at 0.25 m.

Inhomogeneities filled with silt in a background of fine sand are shown in Figure 5, left. The pressure head distributions become structured with two different arrangements observed in the two zones of heterogeneity. Within the upper zone, pressure head decreases in the vertical direction to the gravity drainage pressure head of silt, a value that varies with recharge rate where a larger drop in pressure head occurring across elements with lower recharge rates. It is also observed that, while there is interaction across elements, each element consistently maintains the behavior of the individual element in Figure 3 with an almost one-dimensional increase in pressure head within an element. Within the lower zone, pressure head largely follows that occurring without the presence of inhomogeneities, much like the single object in Figure 4. These patterns of change in pressure head impact the trajectories of water particles in the heterogeneous media similarly to the single inhomogeneities. Pathlines converge within objects at higher elevations as the silt inclusions have higher hydraulic conductivity than the fine sand background, and they diverge around objects at lower elevations near the groundwater table.

Inhomogeneities filled with coarse sand in a fine sand background are shown in Figure 5, right and also exhibit different patterns in the two zones. The pressure head increases within inhomogeneities in the upper zone as it transitions toward the higher values associated with gravity drainage of coarse sand. And yet even within the larger inclusions, pressure head only fluctuates within a small range about the p_0 of the background fine sand as in Figure 3. Near the groundwater table in the lower zone, the pressure head follows the one-dimensional pattern observed near the single inclusion in Figure 4. Pathlines follow the observations from one inhomogeneity as they diverge around objects except for very near the groundwater table, where they become drawn into elements by their higher conductivities there.

The role of hydraulic conductivity in the distribution of pathlines can be deduced from analysis of the $K(p)$ curves in Figure 3. Two red markers are shown where the curve for the background fine sand crosses that for silt at $p = -1.30$ m and for coarse sand at $p = -0.18$ m. These conditions represent an altered state across which the relative values of the soils across each interface take on different rank. This transition for the silt filled inhomogeneities occurs toward the top of the lower zone, where their conductivity is larger than the background above this elevation with pathlines converging within inhomogeneities, and conductivity is lower below with pathlines diverging around them. This transition for the coarse sand filled inhomogeneities occurs nearer the saturated groundwater table, with pathlines diverging around elements throughout most of the domain. Thus, pathlines follow the changes in $K(p)$ occurring as finer grained material become more conductivity than the background at lower pressure head and as coarser grained material become less conductive than the background.

Pathlines exhibit intricate patterns as they flow through and around inclusions in the heterogeneous medium. They become particularly focused with preferential flow paths occurring between closely placed adjacent objects in regions with lower values of $K(p)$. And yet pathlines follow very similar patterns in Figure 5 with only small variations observed in their relative positions between plots with the same soil structure but with shifts in recharge rate. So if shifts in the rate of recharge are not easily discernible through changes in the distribution of pathlines, what can be learned from the pressure head distributions to contribute toward this endeavor?

3.4. Detecting Shifts in Recharge Through Its Corresponding Shift in Pressure Head

It is evident in Figure 5 that the pressure head variation within the vadose zone is impacted by the recharge rate. This is observed in the change of gravity drainage for the fine sand, where p_0 varies with R in (16). And finer differences in the pressure head distributions exist that are difficult to discern in this figure. These details, however, become evident by analyzing the differences in pressure head occurring across a shift in recharge, which is plotted in Figure 6. Each plot is obtained by subtracting the pressure head in Figure 5 at two different values of R for the same soil structure, and the contour interval is reduced to 0.01 m.

Pressure head above the groundwater table in the lower zone follows a one-dimensional progression close to that of fine sand in the middle plots. Here the difference Δp is zero at $z = 0$, and it is equal to the corresponding change in p_0 , (16), at higher elevations, and a transition zone exists between these values (from $z \approx 1$ to 2 m). Within the lower zone, the progression of pressure head toward the fine sand's gravity drainage occurs also for the other soils, with small differences observed in larger coarse sand objects where a faster transition to this value occurs.

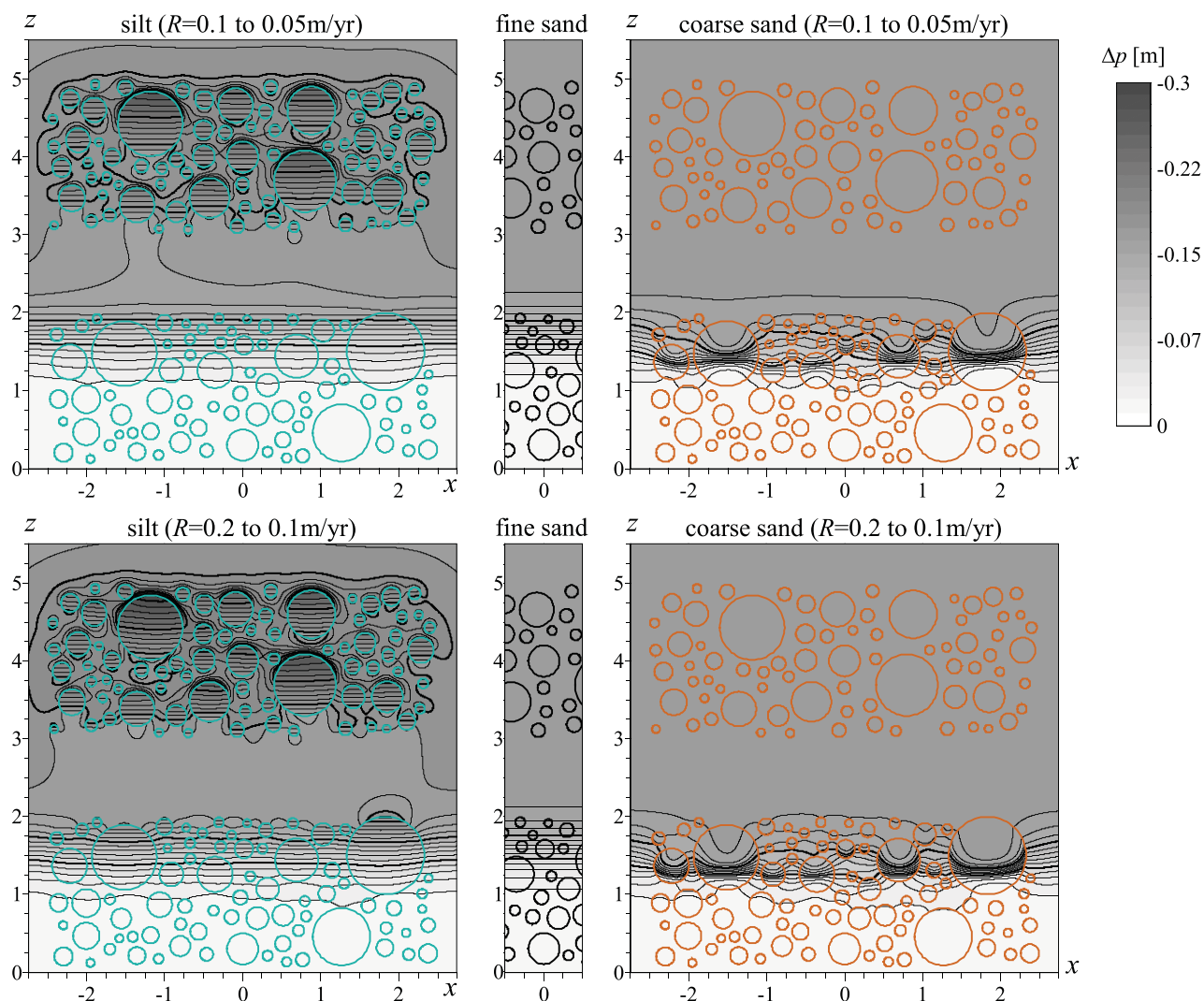


Figure 6. Differences in pressure head across changes in recharge. Contour intervals are 0.01 m with thicker lines at 0.05 m.

The pressure head from shifts in recharge exhibit different patterns for each soil type within the upper zone. Here the pressure head decreases in the finer grained inclusions in Figure 5 at different rates depending upon recharge. This is evidenced in Figure 6 by an almost linear variation in Δp with elevation within each element, and abrupt changes occur across their interfaces with the surrounding soil. And the same patterns emerge by either halving or doubling recharge. The realization of differences in pressure head for the coarse sand inclusions is shown in Figure 6, right. In the upper zone, there is no detectable variation in Δp . The pressure head is reduced in the coarse sand inhomogeneities by the same magnitude as in the surrounding soil.

These results reveal a second intriguing phenomenon: the differences in pressure head distribution occurring due to a shift in recharge is completely controlled by the geometry and conductivity contrasts for coarser grained material embedded in a finer background soil, not by the actual fluxes moving through the system. While inhomogeneities individually and collectively impact the pressure head distribution in Figures 3 and 5, the difference in pressure head occurring due to a shift of recharge is everywhere the same in the upper zone. Consequently, instrumentation to measure pressure head in this region could detect the presence of a coarser grained inclusion by a difference from the background soil. However, observation of change in pressure head is not capable of detecting shifts in recharge rate; the same net change occurs everywhere here. This is contrary to what occurs when a finer grained material is embedded in the background soil. In this case, observations of pressure head could detect both the presence of an

inhomogeneity (Figures 3 and 5) and shifts in recharge (Figure 6). In the zone near groundwater, the same pressure head distribution exists, irregardless of the soil structure and the rate of recharge.

4. Conclusions: Using Heterogeneous Soil Structure to Detect Shifts in Recharge

Nonlinear solution methods are developed to answer the question of how the sorptive number for typical soils impacts recharge through inhomogeneities. This extends linear methods for soils with uniform sorptive number in Figure 1 to those with representative soil properties in Table 1. The nearly exact solutions (Table 2) to the nonlinear interface problem provide a numerical laboratory capable of analyzing the abrupt variations in pressure head and pathlines occurring near interfaces between different soil types. Analysis of pathlines and pressure head identify detectable changes that become manifest across variations in the rate of recharge, as well as patterns that are not impacted. Results from this two-dimensional analysis may be extended to three-dimensional solutions using separation of variables to study the complicated streamlines existing in three-dimensional porous media [Janković *et al.*, 2009].

The impact of soil properties and the vertical placement of an inhomogeneity on pressure head and pathline distributions were studied first. Inclusions with finer or coarser grained material than the background soil type in Figure 3 are shown for representative soil properties within the region of gravity drainage. And, the vertical placement of an inhomogeneity is examined by placing these objects near the groundwater table in Figure 4. These results contribute the understanding that objects near a groundwater table do not influence the pressure head, which take on the same values irregardless of the presence or absence of an inhomogeneity. Although shifts in pathlines may still occur here due to differences in $K(p)$ for different soil types.

The question of how variations in recharge become manifested in a heterogeneous vadose zone was studied using closely juxtaposed inclusions embedded within a uniform background soil. Analysis of results in Figure 5 illustrate that individually, a finer grained soil becomes more conductive in the upper zone of background gravity drainage and less conductive in lower regions; and the opposite effect occurs for a coarser grained inclusion. While pathlines become focused around and through heterogeneity across variations in $K(p)$, only small changes in flow paths occur with shifts in the rate of recharge. Another contribution is the conclusion that no detectable shift in pressure head occurs between a coarser grained material and its finer grained background across a shift in recharge. Instead, changes in pressure head are dominated by the corresponding shift occurring in the background soil. Figure 6 also illustrate that finer grained materials respond differently than the background and provide detectable variations in Δp fields across shifts in recharge. These methods are extensible to other geometric configurations and broader ranges of hydraulic conductivity properties than those of the representative soils in Table 1.

These findings contribute toward the design of instrumentation and interpretation of their data to elucidate the paramount rate of recharge. First, measurements must be collected above the transition zone near groundwater, since the pressure head distribution and corresponding conductivity contrasts are not significantly influenced by changes in recharge. Second, analysis of variations in pressure head in a heterogeneous media is capable of identifying the existence of embedded finer or coarser grained material. Yet such analysis is incapable of determining shifts in recharge from corresponding changes in pressure head for coarse grained soils. Instead, measurement and analysis should focus toward detecting differences occurring between fine grained inclusions and background soil. Quantification of recharge is important in the study of hydrological coupling of surficial and groundwater processes, and the insight from this study provides guidance toward elucidating those parameters that are impacted by changes in recharge rates and those that are not.

Appendix A: Computational Details for the Analytic Element Method

Solutions to seepage through soils in the vadose zone are developed within the framework of the Analytic Element Method [Strack, 1989] and its four steps [Steward and Allen, 2013]. 1) The soil is subdivided into elements with specified geometry in Figure 2. 2) Influence functions, (14) and (17) are developed for each element to satisfy the governing quasilinear equations. 3) A comprehensive solution, (20) and (21), gathers elements and linear superposition of their influence functions. And 4) coefficients are adjusted to match

boundary conditions using (28). Additional details necessary to implement the new nonlinear solution follow.

A1. Computation at Control Points

The function Φ , which needs to be evaluated for the first interface condition, (24), at control point m , is obtained using (20) outside the interface

$$\begin{aligned} \Phi_m^+ &= \sum_{n=0}^N c_n^{K \cos} K_n(k^+ r_0) \cos n\theta_m \\ &+ \sum_{n=1}^N c_n^{K \sin} K_n(k^+ r_0) \sin n\theta_m + \Phi_m^{\text{add}} \end{aligned} \tag{A1a}$$

and (21) inside the interface:

$$\begin{aligned} \Phi_m^- &= \sum_{n=0}^N c_n^{I \cos} I_n(k^- r_0) \cos n\theta_m \\ &+ \sum_{n=1}^N c_n^{I \sin} I_n(k^- r_0) \sin n\theta_m \\ &+ c_1^D e^{-k^- z_m} + c_2^D e^{k^- z_m} \end{aligned} \tag{A1b}$$

where Φ_m^{add} contains the additional functions, (20b), evaluated at this point.

The partial derivative of Φ in the r -direction is also needed for the second interface condition, (27). This is obtained using its gradient for an inhomogeneity (17):

$$\begin{aligned} \frac{\partial \Phi}{\partial x} &= \cos \theta \frac{\partial \Phi}{\partial r} - \frac{\sin \theta}{r} \frac{\partial \Phi}{\partial \theta} \\ \frac{\partial \Phi}{\partial z} &= \sin \theta \frac{\partial \Phi}{\partial r} + \frac{\cos \theta}{r} \frac{\partial \Phi}{\partial \theta} \end{aligned} \tag{A2}$$

where the derivatives outside the element ($r \geq r_0$) are

$$\begin{aligned} \frac{\partial \Phi}{\partial r} &= \sum_{n=0}^N c_n^{K \cos} K_n'(kr) \cos n\theta + \sum_{n=1}^N c_n^{K \sin} K_n'(kr) \sin n\theta \\ \frac{\partial \Phi}{\partial \theta} &= - \sum_{n=0}^N c_n^{K \cos} K_n(kr) n \sin n\theta + \sum_{n=1}^N c_n^{K \sin} K_n(kr) n \cos n\theta \end{aligned} \tag{A3}$$

the derivatives inside ($r < r_0$) are

$$\begin{aligned} \frac{\partial \Phi}{\partial r} &= \sum_{n=0}^N c_n^{I \cos} I_n'(kr) \cos n\theta + \sum_{n=1}^N c_n^{I \sin} I_n'(kr) \sin n\theta \\ \frac{\partial \Phi}{\partial \theta} &= - \sum_{n=0}^N c_n^{I \cos} I_n(kr) n \sin n\theta + \sum_{n=1}^N c_n^{I \sin} I_n(kr) n \cos n\theta \end{aligned} \tag{A4}$$

and the derivatives with respect to r may be obtained from the recursive relations [Abramowitz and Stegun, 1972]

$$\begin{aligned} K_n'(kr) &= \frac{n}{r} K_n(kr) - k K_{n+1}(kr), \\ I_n'(kr) &= \frac{n}{r} I_n(kr) + k I_{n+1}(kr) \end{aligned} \tag{A5}$$

The normal derivative at the control points may be obtained by evaluating

$$\begin{aligned} \frac{\partial \Phi_m^+}{\partial r} &= \sum_{n=0}^N c_n^{K \cos} K_n'(k^+ r_0) \cos n \theta_m \\ &+ \sum_{n=1}^N c_n^{K \sin} K_n'(k^+ r_0) \sin n \theta_m + \frac{\partial \Phi_m^{\text{add}}}{\partial r} \end{aligned} \tag{A6a}$$

$$\begin{aligned} \frac{\partial \Phi_m^-}{\partial r} &= \sum_{n=0}^N c_n^{I \cos} I_n'(k^- r_0) \cos n \theta_m \\ &+ \sum_{n=1}^N c_n^{I \sin} I_n'(k^- r_0) \sin n \theta_m \\ &- c_1^D k^- \sin \theta_m e^{-k^- z_m} + c_2^D k^- \sin \theta_m e^{k^- z_m} \end{aligned} \tag{A6b}$$

where the gradient of the additional functions, (20b), is obtained from the summation of their components (A2) in

$$\frac{\partial \Phi^{\text{add}}}{\partial r} = \cos \theta_m \frac{\partial \Phi^{\text{add}}}{\partial x} + \sin \theta_m \frac{\partial \Phi^{\text{add}}}{\partial z} \tag{A7}$$

A2. Iteration Within Constraints of Soil Properties

During the Newton's iterative solve process, the pressure head must remain negative and real, and this condition in (23) places limitations on possible values of the potential:

$$p \in (-\infty, 0] \rightarrow \begin{cases} \Phi_m^+ \in (0, F_s^+ e^{k^+ z_m}] \\ \Phi_m^- \in (0, F_s^- e^{k^- z_m}] \end{cases} \tag{A8}$$

Iteration begins with an initial estimates $l = 1$ for coefficients that satisfy this criteria by setting

$$\begin{aligned} c_n^{K \cos} |_1 = c_n^{K \sin} |_1 = c_n^{I \cos} |_1 = c_n^{I \sin} |_1 = 0 \\ [e^{-k^- z_m} \quad e^{k^- z_m}] \begin{bmatrix} c_1^D |_1 \\ c_2^D |_1 \end{bmatrix} = \left[(F_s^-)^{\frac{1}{2k^-}} \left(\frac{\Phi_m^{\text{add}}}{F_s^+} \right)^{\frac{1}{2k^+}} \right] \end{aligned} \tag{A9}$$

where the terms Φ_m^{add} in (20b) contain uniform seepage in the vadose zone plus the contributions from all other elements, and this potential is converted into that inside the element using (23). These estimates are used to evaluate the terms in $\mathbf{J}|_1$ and the correction term $\Delta \mathbf{c}|_1$ in (28b). The next estimate for the coefficients is obtained from

$$\mathbf{c}|_{l+1} = \mathbf{c}|_l + \text{SOR} \Delta \mathbf{c}|_l \tag{A10}$$

where SOR is a successive over relaxation factor chosen between 0 and 1 to prevent the Newton's method from overshooting to a value where coefficients give unrealistic values of the potential. For this study, SOR was set to 0.1.

For completeness, the derivative in the Jacobian matrix, (28), are gathered here

$$\frac{\partial f_m^{(1)}}{\partial c_n^{K \cos}} = \left(\frac{e^{-k^+ z_m}}{F_s^+} \right)^{\gamma^+} \frac{\gamma^+ K_n(k^+ r_0) \cos n \theta_m}{(\Phi_m^+)^{1-\gamma^+}} \tag{A11a}$$

$$\frac{\partial f_m^{(2)}}{\partial c_n^{K \cos}} = -e^{-k^+ z_m} [k^+ \sin \theta_m K_n(k^+ r_0) + K_n'(k^+ r_0)] \cos n \theta_m$$

$$\frac{\partial f_m^{(1)}}{\partial c_n^{K \sin}} = \left(\frac{e^{-k^+ z_m}}{F_s^+} \right)^{\gamma^+} \frac{\gamma^+ K_n(k^+ r_0) \sin n \theta_m}{(\Phi_m^+)^{1-\gamma^+}} \tag{A11b}$$

$$\frac{\partial f_m^{(2)}}{\partial c_n^{K \sin}} = -e^{-k^+ z_m} [k^+ \sin \theta_m K_n(k^+ r_0) + K_n'(k^+ r_0)] \sin n \theta_m$$

$$\frac{\partial f_m^{(1)}}{\partial c_n^{I \cos}} = - \left(\frac{e^{-k^- z_m}}{F_s^-} \right)^{\gamma^-} \frac{\gamma^- I_n(k^- r_0) \cos n \theta_m}{(\Phi_m^-)^{1-\gamma^-}} \tag{A11c}$$

$$\frac{\partial f_m^{(2)}}{\partial c_n^{I \cos}} = e^{-k^- z_m} [k^- \sin \theta_m I_n(k^- r_0) + I'_n(k^- r_0)] \cos n \theta_m$$

$$\frac{\partial f_m^{(1)}}{\partial c_n^{I \sin}} = - \left(\frac{e^{-k^- z_m}}{F_s^-} \right)^{\gamma^-} \frac{\gamma^- I_n(k^- r_0) \sin n \theta_m}{(\Phi_m^-)^{1-\gamma^-}} \tag{A11d}$$

$$\frac{\partial f_m^{(2)}}{\partial c_n^{I \sin}} = e^{-k^- z_m} [k^- \sin \theta_m I_n(k^- r_0) + I'_n(k^- r_0)] \sin n \theta_m$$

$$\frac{\partial f_m^{(1)}}{\partial c_1^{1-D}} = - \left(\frac{e^{-k^- z_m}}{F_s^-} \right)^{\gamma^-} \frac{\gamma^- e^{-k^- z_m}}{(\Phi_m^-)^{1-\gamma^-}} \tag{A11e}$$

$$\frac{\partial f_m^{(2)}}{\partial c_1^{1-D}} = 0$$

$$\frac{\partial f_m^{(1)}}{\partial c_2^{1-D}} = - \left(\frac{e^{-k^- z_m}}{F_s^-} \right)^{\gamma^-} \frac{\gamma^- e^{k^- z_m}}{(\Phi_m^-)^{1-\gamma^-}} \tag{A11f}$$

$$\frac{\partial f_m^{(2)}}{\partial c_2^{1-D}} = 2k^- \sin \theta_m$$

Note Φ_m^+ and Φ_m^- in the denominator of these functions are adjusted using (A8) if they stray beyond physically realistic values.

A3. Weighted Newton's Method

The system of equations in (28) may be weighted using

$$\mathbf{J} = \begin{bmatrix} \frac{\partial f_m^{(1)}}{\partial c_n^{K \cos}} & \frac{\partial f_m^{(1)}}{\partial c_n^{K \sin}} & \frac{\partial f_m^{(1)}}{\partial c_n^{I \cos}} & \frac{\partial f_m^{(1)}}{\partial c_n^{I \sin}} & \frac{\partial f_m^{(1)}}{\partial c_1^{1-D}} & \frac{\partial f_m^{(1)}}{\partial c_2^{1-D}} \\ w \frac{\partial f_m^{(2)}}{\partial c_n^{K \cos}} & w \frac{\partial f_m^{(2)}}{\partial c_n^{K \sin}} & w \frac{\partial f_m^{(2)}}{\partial c_n^{I \cos}} & w \frac{\partial f_m^{(2)}}{\partial c_n^{I \sin}} & w \frac{\partial f_m^{(2)}}{\partial c_1^{1-D}} & w \frac{\partial f_m^{(2)}}{\partial c_2^{1-D}} \end{bmatrix}, \tag{A12}$$

$$\mathbf{c} = \begin{bmatrix} c_n^{K \cos} \\ c_n^{K \sin} \\ c_n^{I \cos} \\ c_n^{I \sin} \\ c_1^{1-D} \\ c_2^{1-D} \end{bmatrix}, \quad \mathbf{f} = \begin{bmatrix} f_m^{(1)} \\ w f_m^{(2)} \end{bmatrix}$$

The weight w is used to provide balance between the importance of the $f_m^{(1)}$ conditions on continuity of the pressure head and the $f_m^{(2)}$ specific discharge conditions. For the cases in this study, $w = 1$, however a more accurate solution is obtained by setting $w > 1$ for conditions where flow rates become very small.

Many of the terms in the matrices become very large or very small, particularly for elements with large radius r_0 and high order N . This problem is resolved by rearranging terms between the derivative terms in the Jacobian matrix \mathbf{J} and the coefficients \mathbf{c} to scale each column in the Jacobian by the maximum absolute value of all coefficients within the column so the scaled columns each vary within ± 1 :

$$\mathbf{J} = \begin{bmatrix} \left(\frac{\partial f_m^{(1)}}{\partial C_n} \right)_{\frac{K \cos}{W_n}} & \left(\frac{\partial f_m^{(1)}}{\partial C_n} \right)_{\frac{K \sin}{W_n}} & \left(\frac{\partial f_m^{(1)}}{\partial C_n} \right)_{\frac{I \cos}{W_n}} & \left(\frac{\partial f_m^{(1)}}{\partial C_n} \right)_{\frac{I \sin}{W_n}} & \left(\frac{\partial f_m^{(1)}}{\partial C_n} \right)_{\frac{1^D}{W_n}} \\ \left(\frac{\partial f_m^{(2)}}{\partial C_n} \right)_{\frac{K \cos}{W_n}} & \left(\frac{\partial f_m^{(2)}}{\partial C_n} \right)_{\frac{K \sin}{W_n}} & \left(\frac{\partial f_m^{(2)}}{\partial C_n} \right)_{\frac{I \cos}{W_n}} & \left(\frac{\partial f_m^{(2)}}{\partial C_n} \right)_{\frac{I \sin}{W_n}} & \left(\frac{\partial f_m^{(2)}}{\partial C_n} \right)_{\frac{1^D}{W_n}} \end{bmatrix} \tag{A13}$$

$$\mathbf{c} = \begin{bmatrix} K \cos C_n & K \cos W_n \\ K \sin C_n & K \sin W_n \\ I \cos C_n & I \cos W_n \\ I \sin C_n & I \sin W_n \\ 1^D C_n & 1^D W_n \end{bmatrix}$$

This preconditioning [Van der Vorst, 1992] normalizes the basis functions in \mathbf{J} so each column contains terms between ± 1 .

Iteration continues until only very small changes occur in Φ_m^+ and Φ_m^- across all control points for successive iterates and statistics in Table 2 report accuracy of solution in terms of the average absolute error and root-mean-square error for both $f_m^{(1)}$, (24), and $f_m^{(2)}$, (27). Iteration for each element continued until the rmse of \mathbf{f} in (28) was less than 10^{-12} or the number of iterations becomes $l = 1000$. Gauss-Seidel sequenced through the l elements until changes in Φ_m at all control points for all inhomogeneities was less than 10^{-12} between successive iterates or after 1000 sequences through all elements. It was found that solutions converge more quickly when the l elements are ordered and solved sequentially from lower to higher z_c elevations.

A4. Precomputing Influence Functions at Control Points

The value of functions at control points are evaluated at each iterate, and the speed of evaluation is improved by organizing these computations in matrices with coefficients that may be precomputed before iteration begins. The potential at control points may be computed using

$$\Phi^+ = \begin{bmatrix} \Phi_m^+ \\ \vdots \end{bmatrix}, \Phi^- = \begin{bmatrix} \Phi_m^- \\ \vdots \end{bmatrix}, \Phi^{\text{add}} = \begin{bmatrix} \Phi_m^{\text{add}} \\ \vdots \end{bmatrix}, \partial \Phi^{\text{add}} = \begin{bmatrix} \frac{\partial \Phi_m^{\text{add}}}{\partial r} \\ \vdots \end{bmatrix} \tag{A14}$$

and the coefficients in column vectors

$$\mathbf{c}^{K \cos} = \begin{bmatrix} K \cos C_n \\ \vdots \end{bmatrix}, \mathbf{c}^{K \sin} = \begin{bmatrix} K \sin C_n \\ \vdots \end{bmatrix}, \mathbf{c}^{I \cos} = \begin{bmatrix} I \cos C_n \\ \vdots \end{bmatrix}, \mathbf{c}^{I \sin} = \begin{bmatrix} I \sin C_n \\ \vdots \end{bmatrix}, \mathbf{c}^{1^D} = \begin{bmatrix} 1^D C_1 \\ \vdots \\ 1^D C_2 \end{bmatrix} \tag{A15}$$

and then expressing summations using matrix multiplication with

$$\begin{aligned} \Phi^+ &= \Phi^{K \cos} \mathbf{c}^{K \cos} + \Phi^{K \sin} \mathbf{c}^{K \sin} + \Phi^{\text{add}} \\ \Phi_{mn}^{K \cos} &= [\cos n\theta_m] \begin{bmatrix} K_n(k^+ r_0) & 0 \\ 0 & \ddots \end{bmatrix} \\ \Phi_{mn}^{K \sin} &= [\sin n\theta_m] \begin{bmatrix} K_n(k^+ r_0) & 0 \\ 0 & \ddots \end{bmatrix} \end{aligned} \tag{A16}$$

and

$$\begin{aligned} \Phi^- &= {}^I \Phi \mathbf{c} + {}^I \Phi \mathbf{c} + {}^{1D} \Phi \mathbf{c}, \\ {}^I \Phi_{mn}^{\cos} &= [\cos n\theta_m] \begin{bmatrix} I_n(k^- r_0) & 0 \\ 0 & \ddots \end{bmatrix} \\ {}^I \Phi_{mn}^{\sin} &= [\sin n\theta_m] \begin{bmatrix} I_n(k^- r_0) & 0 \\ 0 & \ddots \end{bmatrix} \\ {}^{1D} \Phi &= [e^{-kz_m} \quad e^{kz_m}] \end{aligned} \tag{A17}$$

Evaluation of the second condition $f_m^{(2)}$ contains the normal component of the vector field outside and inside the element, which is facilitated using matrix multiplication with

$$\begin{aligned} \mathbf{q}_r^+ &= \begin{bmatrix} q_{r_m}^+ \\ \vdots \end{bmatrix} = {}^K \mathbf{q} \mathbf{c} + {}^K \mathbf{q} \mathbf{c} + \alpha_m^+ \Phi + \beta_m^+ \partial \Phi \\ {}^K \mathbf{q}_{mn}^{\cos} &= \begin{bmatrix} \alpha_m^+ & 0 \\ 0 & \ddots \end{bmatrix} [\cos n\theta_m] \begin{bmatrix} K_n(k^+ r_0) & 0 \\ 0 & \ddots \end{bmatrix} + \begin{bmatrix} \beta_m^+ & 0 \\ 0 & \ddots \end{bmatrix} [\cos n\theta_m] \begin{bmatrix} K'_n(k^+ r_0) & 0 \\ 0 & \ddots \end{bmatrix} \\ {}^K \mathbf{q}_{mn}^{\sin} &= \begin{bmatrix} \alpha_m^+ & 0 \\ 0 & \ddots \end{bmatrix} [\sin n\theta_m] \begin{bmatrix} K_n(k^+ r_0) & 0 \\ 0 & \ddots \end{bmatrix} + \begin{bmatrix} \beta_m^+ & 0 \\ 0 & \ddots \end{bmatrix} [\sin n\theta_m] \begin{bmatrix} K'_n(k^+ r_0) & 0 \\ 0 & \ddots \end{bmatrix} \end{aligned} \tag{A18}$$

and

$$\begin{aligned} \mathbf{q}_r^- &= \begin{bmatrix} q_{r_m}^- \\ \vdots \end{bmatrix} = {}^I \mathbf{q} \mathbf{c} + {}^I \mathbf{q} \mathbf{c} + {}^{1D} \mathbf{q} \mathbf{q} \\ {}^I \mathbf{q}_{mn}^{\cos} &= \begin{bmatrix} \alpha_m^- & 0 \\ 0 & \ddots \end{bmatrix} [\cos n\theta_m] \begin{bmatrix} I_n(k^- r_0) & 0 \\ 0 & \ddots \end{bmatrix} + \begin{bmatrix} \beta_m^- & 0 \\ 0 & \ddots \end{bmatrix} [\cos n\theta_m] \begin{bmatrix} I'_n(k^- r_0) & 0 \\ 0 & \ddots \end{bmatrix} \\ {}^I \mathbf{q}_{mn}^{\sin} &= \begin{bmatrix} \alpha_m^- & 0 \\ 0 & \ddots \end{bmatrix} [\sin n\theta_m] \begin{bmatrix} I_n(k^- r_0) & 0 \\ 0 & \ddots \end{bmatrix} + \begin{bmatrix} \beta_m^- & 0 \\ 0 & \ddots \end{bmatrix} [\sin n\theta_m] \begin{bmatrix} I'_n(k^- r_0) & 0 \\ 0 & \ddots \end{bmatrix} \\ {}^{1D} \mathbf{q} &= [k^- \sin \theta_m e^{-k^- z_m} \quad -k^- \sin \theta_m e^{k^- z_m}] \end{aligned} \tag{A19}$$

Acknowledgments

The author gratefully acknowledges financial support provided by the United States Department of Agriculture/Agriculture Research Service (Ogallala Aquifer Project). Data identified in Table 1 are available at the specified references.

References

Abramowitz, M., and I. A. Stegun (1972), *Handbook of Mathematical Functions*, Dover, New York.

Ahring, T. S., and D. R. Steward (2012), Groundwater surface water interactions and the role of phreatophytes in identifying recharge zones, *Hydrol. Earth Syst. Sci.*, 16(11), 4133–4142, doi:10.5194/hess-16-4133-2012.

Bakker, M., and J. L. Nieber (2004a), Analytic element modeling of cylindrical drains and cylindrical inhomogeneities in steady two-dimensional unsaturated flow, *Vadose Zone J.*, 3, 1038–1049.

Bakker, M., and J. L. Nieber (2004b), Two-dimensional steady unsaturated flow through embedded elliptical layers, *Water Resour. Res.*, 40, W12406, doi:10.1029/2004WR003295.

Bernoulli, D. (1738), *Hydrodynamica, sive de viribus et motibus fluidorum commentarii [in Latin]*, Johannis Reinholdi Dulseckeri, Argentorati, France.

Bresler, E. (1978), Analysis of trickle irrigation with application to design problems, *Irrig. Sci.*, 1(1), 3–17.

Courant, R. (1950), *Dirichlet's Principle, Conformal Mapping, and Minimal Surfaces*, Interscience, New York.

Dagan, G. (1979), Models of groundwater flow in statistically homogeneous porous formations, *Water Resour. Res.*, 15(1), 47–63.

Darcy, H. (1856), *Les fontaines publiques de la Ville de Dijon*, Dalmont, Paris.

Gardner, W. R. (1958), Some steady-state solutions of the unsaturated moisture flow equation with application to evaporation from a water table, *Soil Sci.*, 85, 228–232.

Janković, I., and R. J. Barnes (1999), High-order line elements in modeling two-dimensional groundwater flow, *J. Hydrol.*, 226(3–4), 211–223.

Janković, I., D. R. Steward, R. J. Barnes, and G. Dagan (2009), Is transverse macrodispersivity in three-dimensional transport through isotropic heterogeneous formation equal to zero? A counterexample, *Water Resour. Res.*, 45, W08415, doi:10.1029/2009WR007741.

- Khaleel, R., and J. F. Relyea (2001), Variability of Gardner's α for coarse-textured sediments, *Water Resour. Res.*, 37(6), 1567–1575.
- Kirchhoff, G. (1894), *Vorlesungen über der theorie der wärme*, Leipzig, Barth, Germany.
- Knight, J. H., J. R. Philip, and R. T. Waechter (1989), The seepage exclusion problem for spherical cavities, *Water Resour. Res.*, 25(1), 29–37.
- Kuhlman, K. L., and A. W. Warrick (2008), Quasilinear infiltration from an elliptical cavity, *Adv. Water Resour.*, 31(8), 1057–1065.
- Moon, P., and D. E. Spencer (1961), *Field Theory for Engineers*, D. Van Nostrand, Princeton, N. J.
- Philip, J. R. (1968), Steady infiltration from buried point sources and spherical cavities, *Water Resour. Res.*, 4(3), 1039–1047.
- Philip, J. R. (1990), Conjectures on certain boundary-layer equations and natural coordinates, *Proc. R. Soc. London, Ser. A*, 428(1875), 307–324.
- Philip, J. R., J. H. Knight, and R. T. Waechter (1989a), Unsaturated seepage and subterranean holes: Conspectus, and exclusion problem for circular cylindrical cavities, *Water Resour. Res.*, 25(1), 16–28.
- Philip, J. R., J. H. Knight, and R. T. Waechter (1989b), The seepage exclusion problem for parabolic and paraboloidal cavities, *Water Resour. Res.*, 25(4), 605–618.
- Pullan, A. J. (1990), The quasilinear approximation for unsaturated porous media flow, *Water Resour. Res.*, 26(6), 1219–1234.
- Raats, P. A. C., and W. R. Gardner (1974), Movement of water in the unsaturated zone near a water table, in *Agron. Monogr.* 17, chap. 13, pp. 311–357, Am. Soc. of Agron., Madison, Wis.
- Richards, L. A. (1931), Capillary conduction of liquids through porous mediums, *Physics*, 1, 318–333.
- Rockhold, M. L., C. S. Simmons, and M. J. Fayer (1997), An analytic solution technique for one-dimensional, steady vertical water flow in layered soils, *Water Resour. Res.*, 33(4), 897–902.
- Rucker, D. F., A. W. Warrick, and T. P. A. Ferré (2005), Parameter equivalence for the Gardner and van Genuchten soil hydraulic conductivity functions for steady vertical flow with inclusions, *Adv. Water Resour.*, 28, 689–699, doi:10.1016/j.advwatres.2005.01.004.
- Steward, D. R. (2015), Analysis of discontinuities across thin inhomogeneities, groundwater/surface water interactions in river networks, and circulation about slender bodies using slit elements in the Analytic Element Method, *Water Resour. Res.*, 51(11), 8684–8703, doi:10.1002/2015WR017526.
- Steward, D. R., and A. J. Allen (2013), The Analytic Element Method for rectangular gridded domains, benchmark comparisons and application to the High Plains Aquifer, *Adv. Water Resour.*, 60, 89–99, doi:10.1016/j.advwatres.2013.07.009.
- Steward, D. R., X. Yang, S. Y. Lauwo, S. A. Staggenborg, G. L. Macpherson, and S. M. Welch (2011), From precipitation to groundwater baseflow in a native prairie ecosystem: A regional study of the Konza LTER in the Flint Hills of Kansas, USA, *Hydrol. Earth Syst. Sci.*, 15, 3181–3194, doi:10.5194/hess-15-3181-2011.
- Strack, O. D. L. (1989), *Groundwater Mechanics*, Prentice Hall, Englewood Cliffs, N. J.
- Strack, O. D. L. (2003), Theory and applications of the Analytic Element Method, *Rev. Geophys.*, 41(2), 1005, doi:10.1029/2002RG000111.
- Van der Vorst, H. A. (1992), BI-CGSTAB: A fast and smoothly converging variant of BI-CG for the solution of nonsymmetric linear systems, *SIAM J. Sci. Stat. Comput.*, 13(2), 631–644.
- Varado, N., I. Braud, P. J. Ross, and R. Haverkamp (2006), Assessment of an efficient numerical solution of the 1D Richards' equation on bare soil, *J. Hydrol.*, 323, 244–257.
- Warrick, A. W., and J. H. Knight (2002), Two-dimensional unsaturated flow through a circular inclusion, *Water Resour. Res.*, 38(7), doi:10.1029/2001WR001041.
- Warrick, A. W., and J. H. Knight (2004), Unsaturated flow through a spherical inclusion, *Water Resour. Res.*, 40(5), W05101, doi:10.1029/2003WR002890.
- Wooding, R. A. (1968), Steady infiltration from a shallow circular pond, *Water Resour. Res.*, 4(6), 1259–1273.
- Zhu, J., and A. W. Warrick (2012), Unsaturated hydraulic conductivity of repeated layered soil structures, *Soil Sci. Soc. Am. J.*, 76(1), 28–35, doi:10.2136/sssaj2011.0028.